ACS APPLIED MATERIALS & INTERFACES

www.acsami.org

Research Article

Corrosion-Resistant Graphene-Based Magnetic Composite Foams for Efficient Electromagnetic Absorption

Shuangshuang Li, Xinwei Tang, Yawei Zhang, Qianqian Lan, Zhiwei Hu, Le Li, Nan Zhang, Piming Ma, Weifu Dong, Wengweei Tjiu, Zicheng Wang,* and Tianxi Liu*

Cite This: *ACS Appl. Mater. Interfaces* 2022, 14, 8297−8310

Read Online

ACCESS | Metrics & More | Article Recommendations | Supporting Information

ABSTRACT: Designing and fabricating high-performance microwave absorption materials with efficient electromagnetic absorption and corrosion resistance becomes a serious and urgent concern. Herein, novel corrosion-resistant graphene-based carbon-coated iron (Fe@C) magnetic composite foam is fabricated via self-assembly of iron phthalocyanine/Fe_3O_4 (FePc hybrid) on the graphene skeletons under solvothermal conditions and then annealing at high temperature. As a result, the rational construction of a hierarchical impedance gradient between graphene skeletons and Fe@C particles can facilitate the optimization in impedance matching and attenuation characteristic of the foam, realizing the efficient dissipation for incident electromagnetic waves. Additionally, the performance of electromagnetic absorption can be controllably regulated by optimizing annealing temperature and/or time. More importantly, the formation of a carbon-coated iron structure substantially improves the corrosion resistance of magnetic particles, endowing the composite foam with excellent stability and durability in microwave absorption performance.

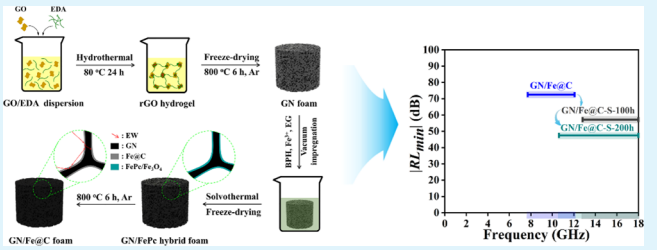

KEYWORDS: *corrosion resistance, graphene, carbon-coated iron, foam, electromagnetic absorption*

INTRODUCTION

With the widespread applications of electronic communication technology, undesirable electromagnetic radiation becomes a more serious pollution source to interfere the adjacent electronic devices and/or damage human health. Therefore, designing and fabricating high-performance microwave absorption (MA) materials with excellent absorption capacity and bandwidth becomes a significant and urgent concern in contemporary society. Over the past decades, various materials, including ferrites, carbonyl iron, and ceramics, were successfully prepared as high-performance microwave absorbers. However, many limitations such as high density, high cost, and low corrosive resistance in a harsh environment heavily hindered their popularization in the domain of MA.[1−4]

As a candidate, carbon-based nanomaterials, especially graphene-based materials, attracted increasing interest and became more efficient MA materials owing to the stable two-dimensional (2D) carbon nanostructure, high specific surface area, low density, and outstanding electrical conductivity.[5−9] As reported by Liu et al., CoS_2 nanoparticles and CoS_2/reduced graphene oxide (CoS_2/rGO) nanohybrids were fabricated by a unique single-mode microwave-assisted hydrothermal method.[7] The minimum reflection loss (RL_{min}) of −56.9 dB was achieved at 10.9 GHz for a thickness of 2.2 mm. Meanwhile, the corresponding effective absorption bandwidth (EAB, reflection loss < −10 dB) of 4.1 GHz was obtained in the frequency range of 9.1−13.2 GHz. Yuan et al. synthesized Fe_3O_4-intercalated reduced graphene oxide (Fe_3O_4-rGO) nanocomposites by an in situ reduction process.[8] Also, the reflection loss revealed that the minimum loss was −49.53 dB at 6.32 GHz for a thickness of 3.4 mm, while the maximum of EAB (EAB_{max}) was 2.96 GHz. In past decades, many significant progresses were made to construct macroscopic three-dimensional (3D) porous architectures from 2D graphene nanosheets.[10−14] Owing to the formation of a porous conductive network, electromagnetic reflection/scattering repeatedly occurs at the internal interfaces of 3D architectures, leading to more electromagnetic waves to be dissipated in the form of multiple reflection/scattering loss. For example, Chen et al. prepared a kind of porous graphene microflowers (Gmf's). The RL_{min} of Gmf's reached to −42.9 dB at 7.1 GHz and the corresponding EAB was 5.59 GHz, revealing substantial increase contrasted with stacked graphene.[12] Zhou et al. prepared recoverable aramid nanofiber/reduce graphene oxide/polyimide (ANF/rGO/PI) composite aerogels by freeze-drying and annealing. The RL_{min} of the sample was up

Received: December 3, 2021
Accepted: January 20, 2022
Published: February 8, 2022

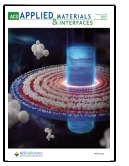

https://doi.org/10.1021/acsami.1c23439
ACS Appl. Mater. Interfaces 2022, 14, 8297−8310

to −41.0 dB at 10.8 GHz and a broad EAB covered the entire X-band.[14]

In order to further enhance the attenuation ability of electromagnetic waves entering the porous conductive networks, many efforts were also devoted to incorporate porous graphene-based materials with magnetic particles in recent years.[15−21] For instance, Xu et al. fabricated three-dimensional magnetic graphene foam decorated with ultrafine Ni nanocrystals (GA@Ni). The magnetic aerogels revealed an excellent RL_{min} value of −52.3 dB at 11.9 GHz.[16] Zhang et al. synthesized the Fe_3O_4/MWCNT/GF composites via the in situ solvothermal reaction.[20] The RL_{min} value of −35.30 dB and 9.01 GHz bandwidth with RL below −10 dB can be easily achieved. Zhao et al. developed an innovative CoNi/reduced graphene oxide (rGO) aerogel via a facile solvothermal and carbonization process.[21] The CoNi/rGO aerogel obtained a high RL_{min} value of −53.3 dB at 16.2 GHz and a narrow EAB value of ∼3.5 GHz. However, it is worthy to note that many magnetic particles were loaded on the external surface of porous skeletons. The magnetic particles were directly exposed to the air owing to the absence of external protecting shells such as carbon, ceramics, or polymer matrix. As a result, those magnetic particles were easily oxidized and/or corroded in the harsh environment, seriously degrading the stability and durability of MA performance. Therefore, the construction of an external protecting shell for magnetic particles becomes necessary to isolate the undesired corrosion.[22−26] As reported by Du et al., core−shell Fe_3O_4@C microspheres were successfully fabricated through in situ polymerization of phenolic resin on the Fe_3O_4 surface and subsequent high-temperature carbonization.[25] When the absorber thickness of the composite was controlled at 2 mm, the optimal RL_{min} value was up to −20.06 dB and the EAB reached to 2.7 GHz (10.9−13.6 GHz). Xiang et al. also synthesized a kind of metal−organic framework-derived Fe_3O_4@carbon (Fe_3O_4@NPC) composites with a strong RL_{min} of −65.5 dB and a wide EAB of 4.5 GHz.[26] However, to date, how to realize the rational construction of the external protecting shell of magnetic particles on porous skeletons is still a huge challenge.

In this paper, we report a simple and effective method to fabricate corrosion-resistant graphene-based carbon-coated iron (Fe@C) magnetic composite foams via self-assembly of iron phthalocyanine/Fe_3O_4 (FePc hybrid) on graphene skeletons under solvothermal conditions and then annealing at high temperature. As a unique aromatic heterocyclic macromolecule with a metal ligand, the in situ pyrolysis of rigid FePc molecules combined with Fe_3O_4 nanoparticles in hybrids can effectively facilitate the formation of core−shell carbon-coated iron (Fe@C) particles in the high annealing temperature. As a result, the successful construction of a hierarchical impedance gradient between graphene skeletons and Fe@C particles can further facilitate the optimization in impedance matching of graphene foams, promoting more incident electromagnetic waves to enter the absorber. Furthermore, the formation of Fe@C magnetic particles further enhances the attenuation characteristic for electromagnetic waves entering the foam due to the generation of more interface polarization, dipole polarization, and magnetic loss, realizing the efficient dissipation for incident electromagnetic energy. More importantly, the formation of a core−shell carbon-coated iron structure substantially improves the oxidation and/or corrosion resistance of iron magnetic particles, thereby endowing the composite foam with excellent stability and durability in MA performance.

EXPERIMENTAL SECTION

Materials. The GO powder was prepared via an improved Hummers' method as reported previously.[11,13] Bis-phthalonitrile (BPH) was prepared in our laboratory,[27] which was described in Figure S1 in detail. Ethanediamine (EDA), ethylene glycol (EG), polyethylene glycol (PEG-2000), sodium acetate (NaAc), and iron (III) chloride hexahydrate ($FeCl_3·6H_2O$, ≥99.0%) were purchased from Sinopharm Chemical Reagent Co., Ltd. All reagents used in our experiments were purchased and used as received without further purification.

Preparation of Graphene Foam. GO powder (40 mg) was homogeneously dispersed into 10 mL of deionized water by vigorous stirring and sonication for 30 min, which was then blended with 0.1 g of EDA as a cross-linking agent. After forcefully stirring, the homogeneous suspension was sealed in a glass vial and heated at 80 °C 24 h without stirring. Then, the as-prepared rGO hydrogel was dialyzed with deionized water to remove residual EDA. The rGO foam can be first acquired by freeze-drying to remove the remaining water of rGO hydrogel and then annealed at high temperature of 800 °C for 6 h. The final obtained foam was labeled GN.

Preparation of Graphene-Based Magnetic Composite Foam. The graphene-based magnetic composite foam was prepared via a solvent-thermal and annealing route in Figure S2. BPH powder (0.2 g) was homogeneously dispersed into 20 mL of EG by vigorous stirring at 150 °C, followed by the addition of 3.6 g of NaAc as an alkaline modifier, 1 g of PEG-2000 as a thickening agent, and 1.35 g of $FeCl_3·6H_2O$ at a lower temperature. The abovementioned GN foam was vacuum-impregnated into the mixed solution. The mixture was transferred into a Teflon-lined stainless-steel autoclave. The autoclave was seated and maintained at 200 °C for 15 h. The obtained sample was washed with distilled water for removing residual monomers or other ions and then freeze-dried to remove the residual water inside, which was denoted as the GN/FePc hybrid. The resultant foams were annealed at 600, 800, and 1000 °C for 6 h, which were marked as GN/Fe@C-600, GN/Fe@C-800 (GN/Fe@C as a reference without special emphasis), and GN/Fe@C-1000, respectively. As a control, the foams were annealed at 800 °C with different times of 3 h, 6 h, and 9 h, which were named GN/Fe@C-800-3h, GN/Fe@C-800-6h, and GN/Fe@C-800-9h, respectively. The preparation of GN/Fe@C composite foam was illustrated, as shown in Scheme 1.

Characterizations. The morphology of the foams was analyzed by field emission scanning electron microscopy (FE-SEM) at an accelerating voltage of 30 kV. High-resolution transmission electron

Scheme 1. Schematic Illustration of the Preparation of GN/Fe@C Foam

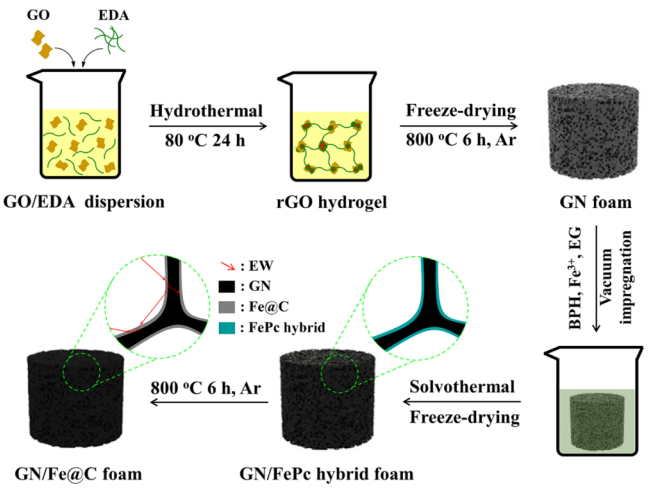

https://doi.org/10.1021/acsami.1c23439
ACS Appl. Mater. Interfaces 2022, 14, 8297−8310

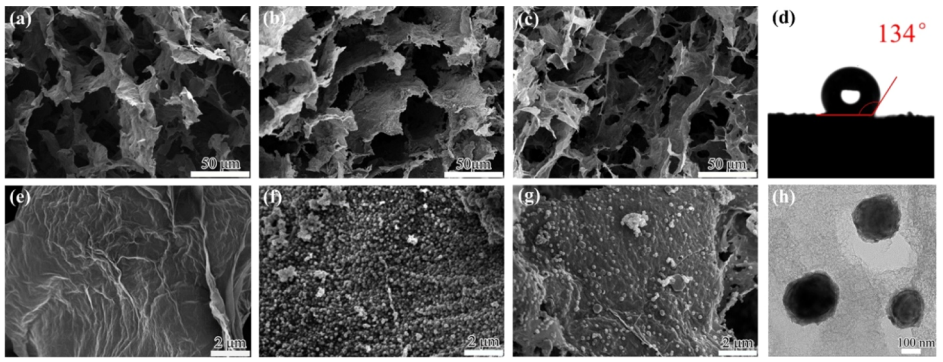

Figure 1. Cross-sectional SEM images of (a,e) GN, (b,f) GN/FePc hybrid, and (c,g) GN/Fe@C; (d) photograph of a water droplet on the surface of GN/Fe@C; and (h) TEM image of GN/Fe@C.

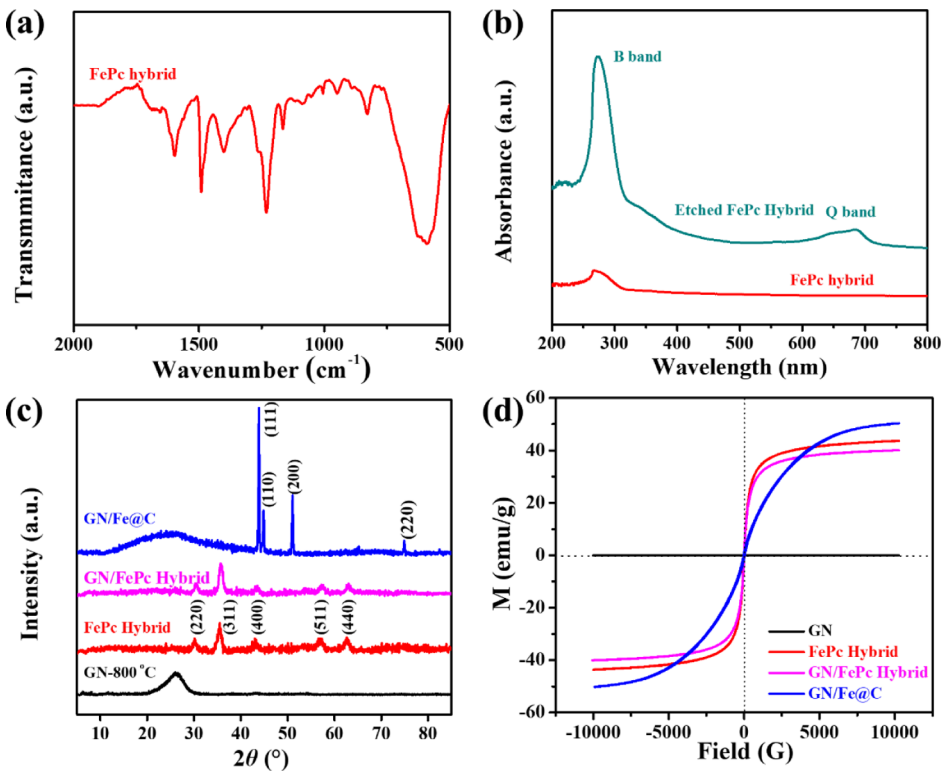

Figure 2. (a) FTIR and (b) UV−vis spectra of the FePc hybrid and (c) XRD and (d) hysteresis loops of GN, FePc hybrid, GN/FePc hybrid, and GN/Fe@C.

microscopy (HR-TEM) was carried out to further identify the microstructure of the samples. Fourier transform infrared spectroscopy (FTIR) was performed using a Nicolet 6700 USA spectrophotometer. Ultraviolet−visible spectrophotometry (UV−vis) spectra were recorded on a UV2501-PC spectrophotometer. X-ray diffraction (XRD) patterns were characterized on a Bruker D8 X-ray diffractometer. The magnetic properties were tested using a magnetic property measurement system (SQUID-VSM) at 300 K. Thermal gravimetric analysis (TGA) was carried out using a TGA/DSC1/1100SF system under a N_2 atmosphere at a heating rate of 10 °C/min. Corrosion tests were performed for assessing the durability of the obtained GN/Fe@C foams in a neutral salt spray chamber. According to GB/T5170.2-96, the specimens were exposed to a 5 wt % NaCl solution for 100 and 200 h at a temperature of 35 °C. The electromagnetic parameters in the 0.5−18.0 GHz were measured using a vector network analyzer (VNA, Agilent 8720ET) to further calculate the MA properties. The testing foams were fabricated by vacuum impregnation with melting paraffin and cut into standard coaxial rings with an outer diameter of 7.0 mm and an inner diameter of 3.0 mm. The percentage of paraffin in the samples was ∼85 wt %.

RESULTS AND DISCUSSION

Structure and Morphology of Composite Foams. The fabrication procedure of GN/Fe@C foam is illustrated in Scheme 1. First, GO can be stably dispersed in aqueous solutions or solvents through static electricity and hydrogen-bonding interactions. After EDA is added in the hydrothermal process, the oxygen functional groups of GO nanosheets are partly removed, and the corresponding conjugated structure of graphene sheets is restored. More importantly, due to the reaction between the epoxy groups of GO and amino groups in EDA on driving force, the addition of ethylenediamine as a cross-linking agent significantly accelerates the formation of an isotropous 3D cross-linked network structure between graphene sheets at 80 °C, endowing graphene with excellent

https://doi.org/10.1021/acsami.1c23439
ACS Appl. Mater. Interfaces 2022, 14, 8297−8310

morphology and mechanical properties. Based on the above-mentioned discussion, GN foam can be obtained by a mild hydrothermal reaction between GO nanosheets and EDA,[28] undirectional freeze-drying, and subsequent thermal treatment. As shown in Figure 1a,e, a cross-linked isotropous microcellular network with cell size beyond several ten microns is successfully constructed in GN foam.

Second, in order to achieve the effective loading of FePc hybrids on the GN skeletons (as shown in Scheme 1), the residual oxygen functional groups on the GN foam after being annealed at 800 °C play a vital role in driving the generation of in situ deposition of the FePc hybrid on GN skeletons through electrostatic interaction with Fe^{3+}. During the solvothermal reaction, BPH as the reactive materials with Fe^{3+} are added into the system (EG) for realizing the in situ synthesis of FePc macromolecules on GN skeletons. Moreover, sodium acetate (NaAc) is added into the system as an alkaline modifier to promote the reduction of Fe^{3+}, resulting in the formation of magnetic Fe_3O_4 nanoparticles in FePc hybrids. Meanwhile, polyethylene glycol (PEG-2000) as a thickening agent is added into the system to restrain the agglomeration and sedimentation of high-density FePc hybrid particles, thereby accelerating the uniform deposition of the FePc hybrid on GN skeletons. As shown in Figure 1b,f, the spherical particles with a diameter of ∼150 nm are effectively prepared and tightly deposited on the smooth surface of GN foam. As a control, the spherical particles are also prepared without GN foam under the same conditions (labeled FePc hybrid) and characterized by FTIR, UV−vis, XRD, VSM, and TGA. As displayed in Figure 2a, a series of FTIR absorption peaks arise at 1596, 1488, 1400, 1163, 1088, and 769 cm^{-1}, which agree well with the characteristic peaks of metal−phthalocyanine skeletal vibrations.[29] The FTIR absorption band located at 588 cm^{-1} may be identified to the characteristic absorption peak of Fe_3O_4.[30] Moreover, the appearance of those X-ray diffraction (XRD) peaks at 30.1, 35.4, 43.1, 56.9, and 62.5° (Figure 2c) confirms the formation of Fe_3O_4 in hybrids, corresponding to (220), (311), (400), (511), and (440) indexed planes of Fe_3O_4 (JCPDS no.75-1609), respectively. Furthermore, it is worthwhile to notice that the UV−vis characteristic absorption B-band (200−300 nm) and Q-band (600−800 nm) of metal phthalocyanine in hybrids are covered up unless Fe_3O_4 is fully etched in 5% HCl (Figure 2b).[31] Meanwhile, it can be clearly seen from Figure S3 that the GN foam is very stable with a little weight loss, while the thermal stability of the sample after solvothermal treatment exhibits an obvious degradation in TGA curves. It can be due to the introduction of unstable organic macromolecules (FePc) in FePc hybrids. Therefore, it can be concluded that the spherical particle is consisted of iron phthalocyanine (FePc) and Fe_3O_4. Also, a strong interaction exists between FePc and Fe_3O_4 in hybrids. As a result, the FePc hybrid particles are successfully loaded on the surface of GN foam, which can be used as an effective carbon and iron source in this system.

After being annealed at 800 °C for 6 h, a similar surface morphology can be observed in Figure 1c,g. However, the micrograph shows a lower density of spherical particles. Meanwhile, the foam exhibits an increased saturation magnetization (Ms) of 50.2 emu/g than that of the GN/FePc hybrid (Figure 2d). The changes could be attributed to the in situ pyrolysis of the FePc hybrid on GN skeletons. The identification of microstructure changes can also be confirmed by XRD and TGA. As shown in Figure S3, the sample annealed at 800 °C 6 h shows a significant improvement in the curves of weight loss in comparison with that of GN/FePc hybrid foam, which confirms the excellent thermal stability. As demonstrated in Figure 2c, the characteristic diffraction peaks of the foam transform from the single Fe_3O_4 in the GN/FePc hybrid to a superposition state, corresponding to the peaks at 44.6° (110), 65.0° (200), and 82.3° (211) of Fe (JCPDS no. 06-0696) and the peaks at 43.9° (111), 51.3° (200), and 75.4° (220) of C (JCPDS no. 43-1104), respectively. For the samples, HR-TEM was also used to further explore the microstructure changes. As shown in Figure S4a,b, spherical particles of the FePc hybrid (∼150 nm) are evenly distributed on the surface of graphene sheets, which is consistent with the result of SEM in Figure 1f. The TEM image at higher magnification (Figure S4b) further indicated that the obtained FePc hybrid particle has a homogeneous and loose structure. After being annealed at 800 °C for 6 h, the micromorphology of the sample exhibits a dramatic evolution, as shown in Figures 1h and S4c,d. It can be obviously seen that a desired core−shell structure is successfully constructed in the particle. Moreover, the d-spacing value (0.204 nm) of the well-defined layered shell (as shown in Figure S5) agrees well with that (0.206 nm) of the characteristic peak indexed to (111) of C (PDF#43-1104) centered at 43.9°. Therefore, we can conclude that the unique core−shell configuration consisted of a carbon-coated iron structure (Fe@C). It can be ascribed to the in situ pyrolysis of the FePc hybrid on GN skeletons. As a unique aromatic heterocyclic macromolecule with a metal ligand, the in situ pyrolysis of rigid FePc molecules combined with the deoxygenation of Fe_3O_4 could provide enough iron source and stable carbon source. Based on this, the respective coalescence of iron atoms and carbon atoms synergistically facilitates the formation of core−shell carbon-coated iron particles in high annealing temperature. As a consequence, the formation of the carbon-coated iron structure plays a vital role in improving the oxidation and/or corrosion resistance of magnetic particles. Furthermore, the higher hydrophobicity with a contact angle of 134° (as displayed in Figure 1d) endows GN/Fe@C foam with an excellent self-cleaning surface due to the formation of an inactive carbon-coated iron structure on the GN skeletons. The self-cleaning surface facilitates the slipping of deliquescent salt particles attached to the surface of foam in a harsh oceanic environment. As a result, it would restrain the corrosion of strong electrolyte solution derived from deliquescent salt,[32] thereby endowing the composite foam with excellent stability and durability in MA performance. More importantly, many holes are also generated around magnetic Fe@C particles, as shown in Figure 1h. It may be attributed to the corrosion of iron particles with high catalytic activity on graphene skeletons during thermal treatment. The intrinsic corrosion would provide more carbon sources to facilitate the formation of Fe@C particles. As a result, the formation of in situ holes on the surface of GN skeletons may contribute to the improvement in MA performance owing to the generation of more dipole defects at the edge of the hole.[33,34]

Electromagnetic Parameters of Composite Foams. In general, the MA performance was closely related to the surface impedance matching and attenuation characteristic of the materials, which were also decided by the permittivity ($\varepsilon_r = \varepsilon' - j\varepsilon''$) and permeability ($\mu_r = \mu' - j\mu''$). To further clarify the effect of material composition and structure on the final MA performance, the electromagnetic parameters of those foams are measured in the frequency range of 0.5−18 GHz. Figures

https://doi.org/10.1021/acsami.1c23439
ACS Appl. Mater. Interfaces 2022, 14, 8297−8310

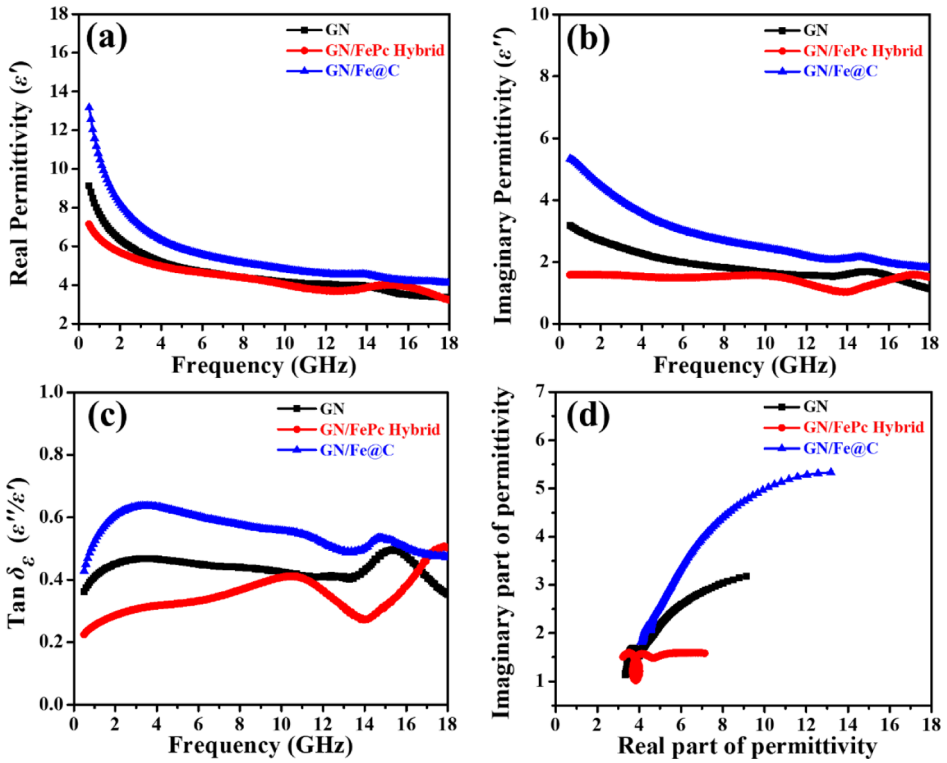

Figure 3. (a) Real parts and (b) imaginary parts of complex permittivity, (c) dielectric loss tangent, and (d) Cole−Cole semicircle of the corresponding foams.

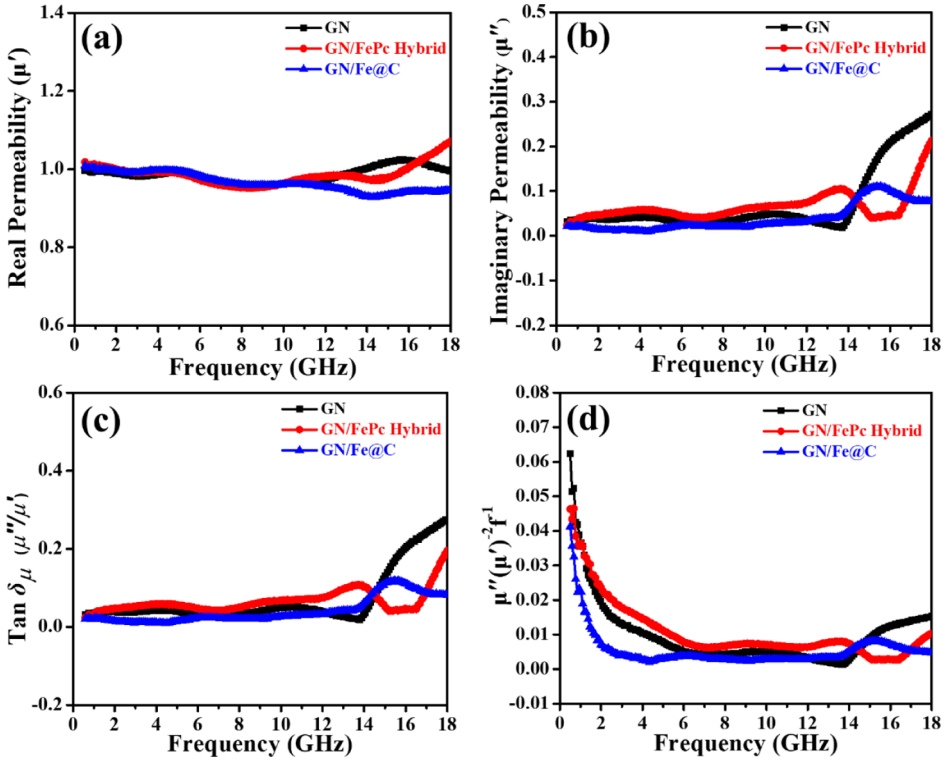

Figure 4. (a) Real parts and (b) imaginary parts of complex permeability, (c) magnetic loss tangent, and (d) C_0 value of the corresponding foams.

3a,b and S6a,b show the real part (ε') and imaginary part (ε'') of complex permittivity for the foams, which represent the storage and loss ability of electric energy, respectively. Because graphene is nonmagnetic, we only analyze the complex permittivity of the graphene foam before (RGO) and after (GN) annealing. As shown in Figure S6a,b, the GN foam shows a tendency to increase in the real and imaginary parts of complex permittivity after annealing. It can be attributed to the effective thermal reduction of graphene sheets during the annealing treatment. However, in comparison with pure GN

https://doi.org/10.1021/acsami.1c23439
ACS Appl. Mater. Interfaces 2022, 14, 8297−8310

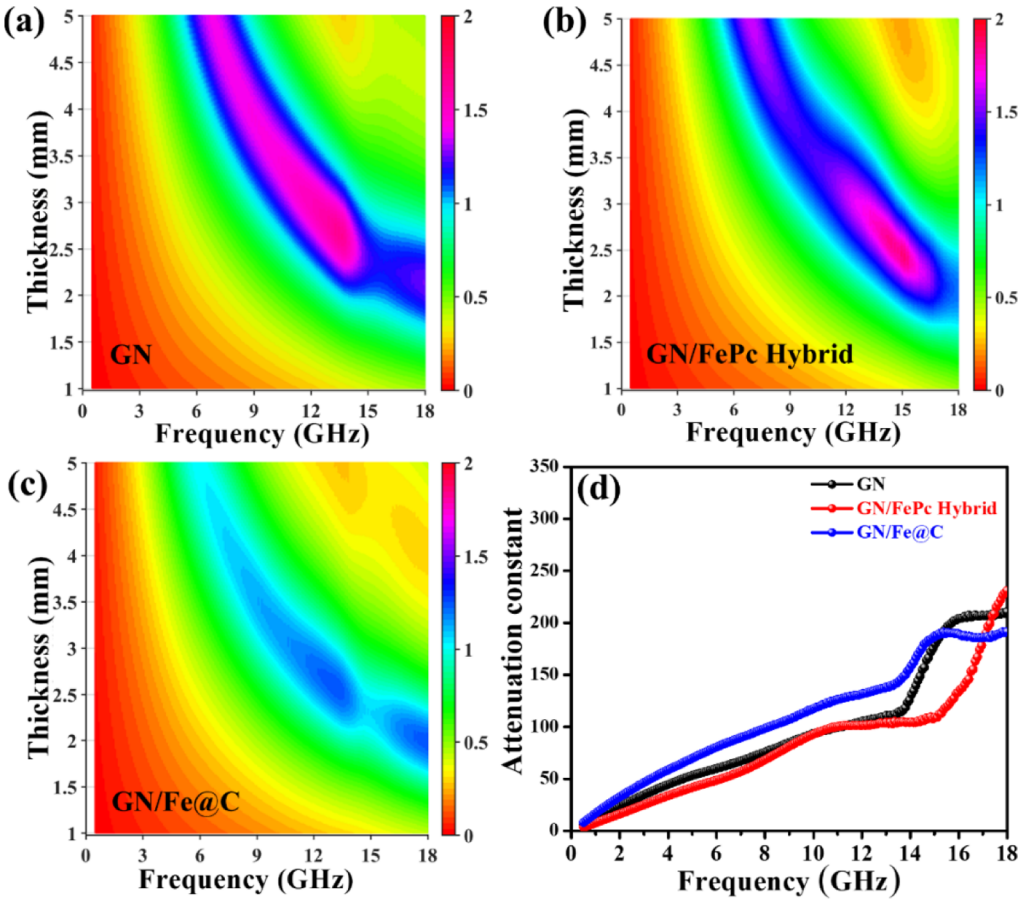

Figure 5. 2D impedance matching contour maps ($|Z_{in}/Z_o|$) of (a) GN, (b) GN/FePc hybrid, and (c) GN/Fe@C and (d) attenuation constant curves of the corresponding foams.

foam, a significant decline of complex permittivity can be obviously seen in the GN/FePc hybrid. It may be due to the introduction of the FePc hybrid with lower permittivity. After being annealed at 800 °C for 6 h, ε' and ε'' of GN/Fe@C exhibit a conspicuous improvement and the dielectric loss tangent ($\tan \delta_\varepsilon = \varepsilon''/\varepsilon'$), as shown in Figure 3c.

On the other hand, the μ' and μ'' values of complex permeability for GN foam, respectively, fluctuate around 1.0 and 0.07 in the frequency range of 0.5−12 GHz, while those of the GN/FePc hybrid exhibit a certain amount of increase in the corresponding frequency, as shown in Figure 4a,b. It indicates the stronger storage and loss abilities of magnetic energy in the GN/FePc hybrid, which once again confirms the successful introduction of a magnetic FePc hybrid. However, compared with traditional magnetic materials, the relative low value of μ' and μ'' for the GN/FePc hybrid may be due to the low content, small size, and Snoek's limitation of the isotropic FePc hybrid in the ultralight foam (9.13 mg/cm^3). After being annealed at 800 °C for 6 h, the μ' and μ'' values of GN/Fe@C foam show an obvious tendency to decrease as compared with those of the GN/FePc hybrid. It may be attributed to the synergistic effect of further reduction of graphene skeletons and in situ pyrolysis of the FePc hybrid. As a consequence, the controllable evolution of complex permittivity and permeability for the composite foams exhibits a promise to become an efficient method for realizing the optimization of impedance matching and attenuation characteristic.

Based on those electromagnetic parameters, the normalized characteristic impedance ($Z = |Z_{in}/Z_o|$) can be calculated to evaluate the impedance matching of the samples according to eq 1

$$Z_{in} = Z_0\sqrt{\frac{\mu_r}{\varepsilon_r}}\tanh\left[j\left(\frac{2\pi fd}{c}\right)\sqrt{\mu_r\varepsilon_r}\right] \quad (1)$$

where Z_{in} and Z_0 are the impedance of samples and vacuum, respectively; μ_r and ε_r are the relative permeability and permittivity of the samples, respectively; d is the thickness of the samples; j is the imaginary unit; f is the frequency of microwaves, and c is the speed of light.[7,8] As a consequence, the two-dimensional (2D) impedance matching contour maps of these samples are shown in Figure 5. The area of sky-blue color in map represents that Z equals 1. As is known, realizing a good impedance matching requires that Z equals or is close to 1. As shown in Figure 5a, the appearance of a large red area in the map reveals the generation of impedance mismatching in GN foam, which can be attributed to the existence of an interconnected 3D conductive graphene network. Compared with pure GN and GN/FePc hybrid foam, GN/Fe@C foam with the largest sky-blue area exhibits a conspicuous optimization in impedance matching (Figure 5b,c). The excellent impedance matching can be ascribed to the rational construction of a more suitable impedance gradient between Fe@C particles and GN skeletons than that of the GN/FePc hybrid, allowing more electromagnetic waves to enter the materials.

https://doi.org/10.1021/acsami.1c23439
ACS Appl. Mater. Interfaces 2022, 14, 8297−8310

Scheme 2. Schematic Illustration of the Different Microwave Absorption Mechanisms in GN/Fe@C: (a) Multiple Reflection/Scattering, (b) Conductive Loss, (c) Interface Polarization, (d) Dipole Polarization, and (e) Magnetic Loss

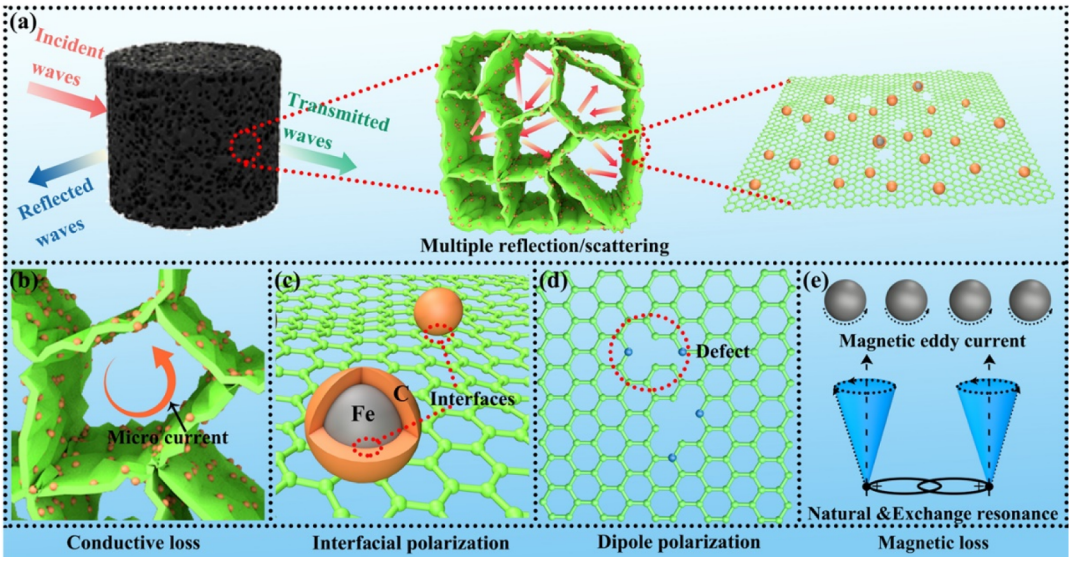

Simultaneously, the attenuation constant was employed to evaluate the electromagnetic energy attenuation ability of the foams, as shown in eq 2

$$\alpha = \frac{\sqrt{2}\pi f}{c} \sqrt{(\mu''\varepsilon'' - \mu'\varepsilon') + \sqrt{(\mu''\varepsilon'' - \mu'\varepsilon')^2 + (\mu''\varepsilon' + \mu'\varepsilon'')^2}} \quad (2)$$

where ε' and ε'' represent the real and imaginary part of complex permittivity, respectively, and μ' and μ'' represent the real and imaginary part of complex permeability, respectively. As depicted in Figure 5d, GN/Fe@C foam exhibits the highest attenuation constant than the pure GN and GN/FePc hybrid foam, suggesting the strongest attenuation ability for incident electromagnetic wave entering the foam.[35−37]

In order to further explore the factors contributing to the attenuation constant, the plots of ε'' versus ε' (dielectric loss and Cole−Cole semicircles) and μ'' versus μ' (magnetic loss tangent and C_0) for the samples are shown in Figures 3c,d and 4c,d, respectively. As for the dielectric loss, there are several dielectric loss peaks and the corresponding Cole−Cole semicircles for GN foam in Figure 3c,d, revealing different Debye relaxation processes. These relaxation processes may be caused by the dipole polarization of abundant defects in GN foam under the altering electromagnetic field (as demonstrated in Scheme 2d). Moreover, it is worth noting that other loss can be confirmed by the presence of the line tail in the curve of GN foam (Figure 3d). It can be identified as the conductive loss originated from interconnected conductive graphene network (Scheme 2b).[38−40] After being incorporated with the FePc hybrid, the plot of GN/FePc hybrid foam exhibits multiple Cole−Cole semicircles distinguished from GN foam. The corresponding relaxation processes might be caused by the interfacial polarization between the GN skeleton and FePc hybrid and FePc and Fe_3O_4 in hybrids, being beneficial to the attenuation of microwave energy. After being annealed at 800 °C for 6 h, the plot of GN/Fe@C displays a more drastic evolution in comparison with that of the GN/FePc hybrid, which is similar to that of pure GN foam (Figure 3d). As to GN/Fe@C, the curve length further extends to a higher position than that of GN, implying the progressive enhancement in dielectric loss and conductive loss. The significant enhancement could be also ascribed to further reduction of graphene skeletons and in situ pyrolysis of the FePc hybrid. Meanwhile, more interfaces can be formed between the Fe core and carbon shell in Fe@C particles and between the GN skeleton and the carbon shell (Scheme 2c). The generation of more interface polarization under an alternating electromagnetic field will further enhance the efficient attenuation of incident electromagnetic waves. As a consequence, the progress in electrical conductivity of the foam, the generation of abundant defects in corroded hole edges (as shown in Figure 1h), and the formation of multiple interfaces jointly promote the efficient dissipation of incident electromagnetic wave as conductive loss, Debye dipole polarization, interfacial polarization, and multiple reflection/scattering between the internal interfaces of the foam skeleton (as depicted in Scheme 2).

As for magnetic loss, the loss form mainly involves magnetic hysteresis, domain wall resonance, eddy current loss, exchange resonance, and natural resonance. In this case, the magnetic hysteresis can be easily excluded because it only appears under a strong applied field. The domain wall resonance occurs in low frequency (<100 MHz); thus, it can also be ignored in the 0.5−18 GHz. Whether the eddy current loss exists can be judged according to eq 3

$$C_0 = \mu''(\mu')^{-2}(f)^{-1} = 2\pi\mu_0 d^2\sigma/3 \quad (3)$$

where μ_o and σ are the permeability of vacuum and the electric conductivity, respectively.[39−41] When there is an eddy current effect, C_0 is a constant as the frequency changed. Otherwise, there are other magnetic losses in the system. As demonstrated in Figure 4d, it is not difficult to find that the C_0 values between the three samples remain constant at 6−14 GHz and fluctuate at other frequency, indicating that the eddy current, natural resonance, and exchange resonance all play a vital role in the magnetic dissipation of electromagnetic energy in this system (as demonstrated in Scheme 2e). Therefore, the aforementioned two main facts, including the dielectric loss

https://doi.org/10.1021/acsami.1c23439
ACS Appl. Mater. Interfaces 2022, 14, 8297−8310

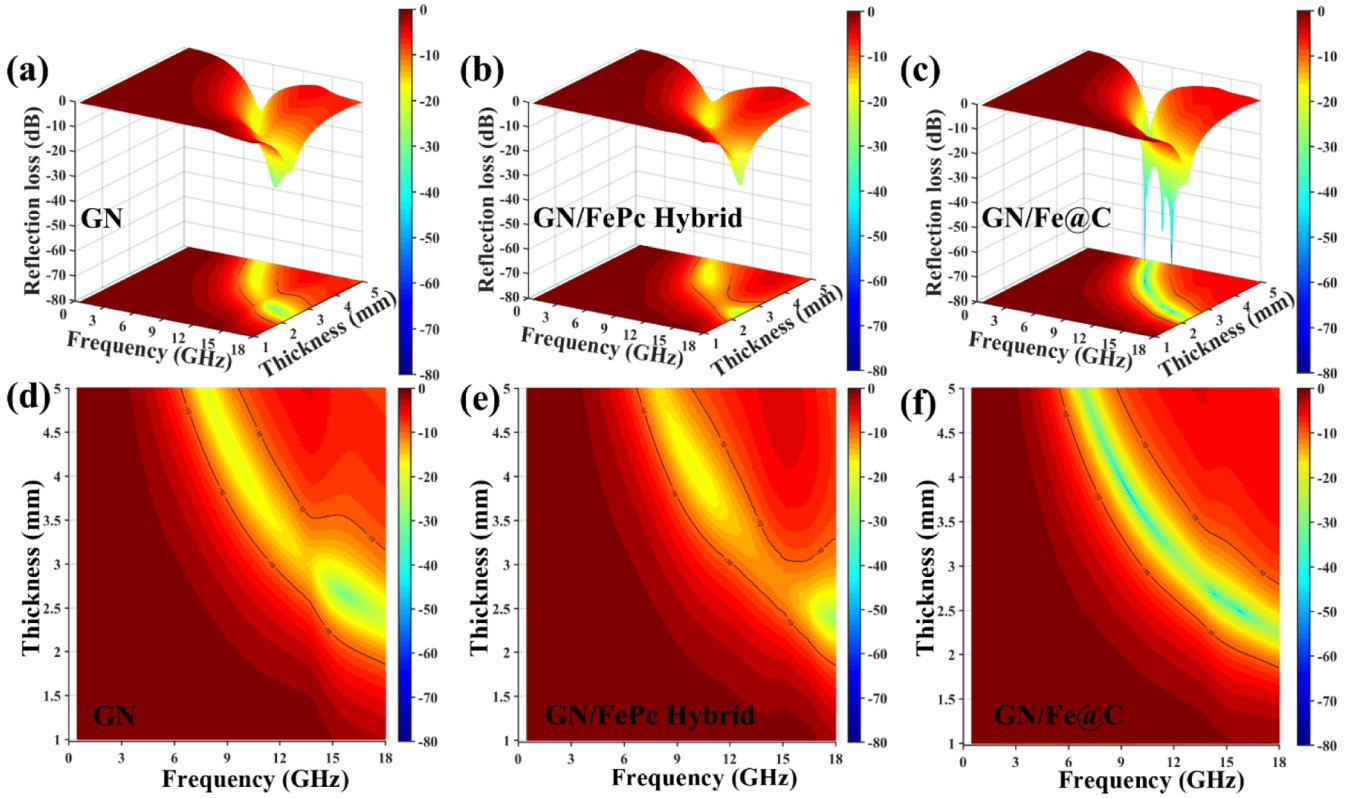

Figure 6. 3D reflection loss and contour maps of the foams with different thickness (1−5 mm) at 0.5−18 GHz: (a,d) GN; (b,e) GN/FePc hybrid; and (c,f) GN/Fe@C composite foam.

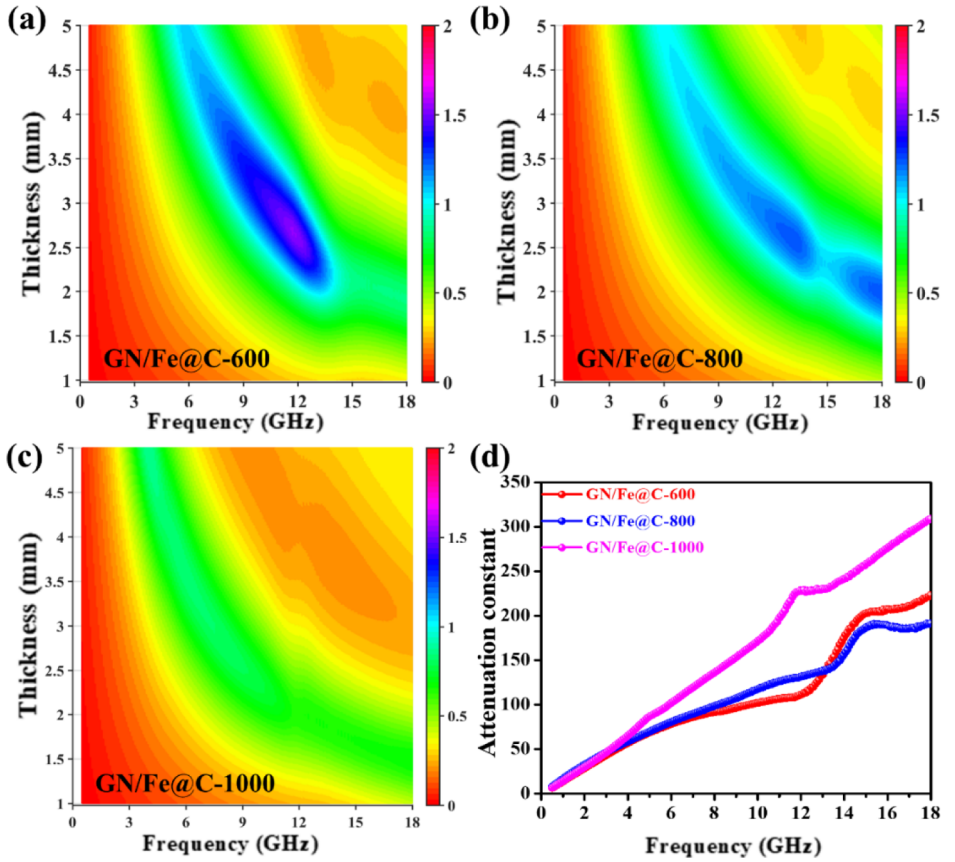

Figure 7. 2D impedance matching contour maps ($|Z_{in}/Z_o|$) of GN/Fe@C annealed at (a) 600, (b) 800, and (c) 1000 °C; (d) attenuation constant curves of the corresponding foams.

https://doi.org/10.1021/acsami.1c23439
ACS Appl. Mater. Interfaces 2022, 14, 8297−8310

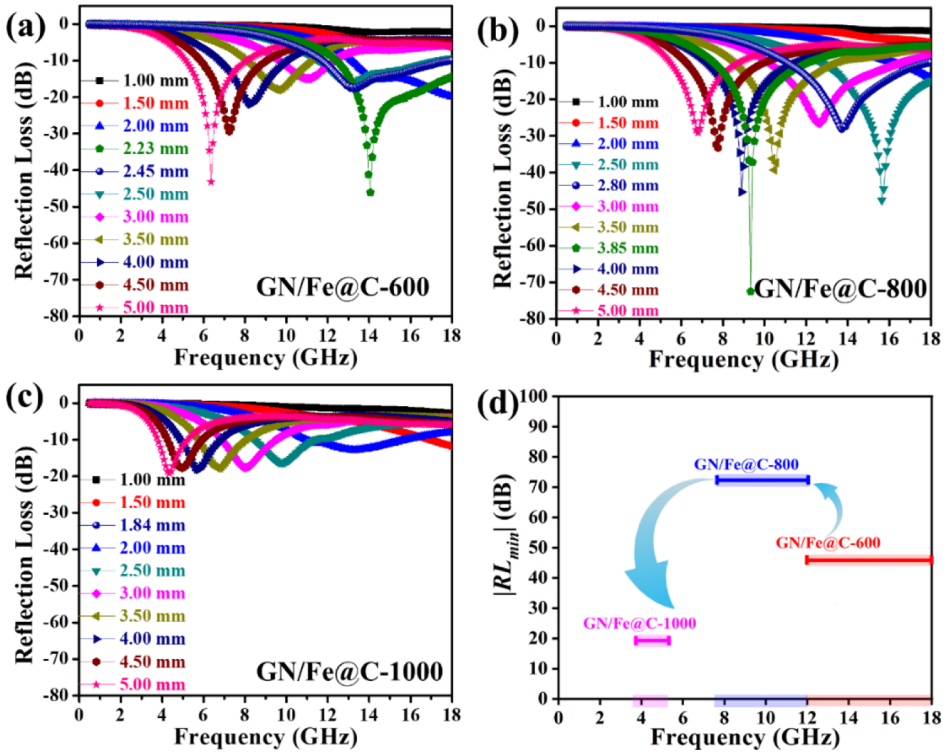

Figure 8. 2D reflection loss maps of GN/Fe@C annealed at (a) 600, (b) 800, and (c) 1000 °C; (d) the summary of MA performance for the corresponding foams.

and magnetic loss, jointly endow the GN/Fe@C foam with excellent attenuation characteristics. Under the synergistic effect of optimized impedance matching and attenuation characteristics for GN/Fe@C foam, more incident electromagnetic waves can be allowed to enter the material and thus dissipated as much as possible after entering the foam.

Microwave Absorption Properties of Composite Foams. In order to further investigate the MA performance of the samples, the reflection loss of incident electromagnetic waves can be calculated by transmission line theory according to eq 4

$$\mathrm{RL(dB)} = 20 \log \left| \frac{Z_{in} - Z_0}{Z_{in} + Z_0} \right| \quad (4)$$

Figure 6 presents the 3D reflection loss and contour maps and the corresponding 2D reflection loss maps of the samples, which are also summarized in Table S1. It can be distinctly observed that GN/Fe@C exhibits a higher MA capability than that of GN and GN/FePc hybrid. As shown in Figures 6a,d, and S6c,d, pure GN shows an RL_{min} of −31.40 dB and an EAB of 4.62 GHz (13.38−18 GHz) as the thickness and frequency are set to 3.15 mm and 15.64 GHz, respectively, which is higher than that of RGO foam. It can be due to the formation of a higher conductive porous network in GN foam after annealing. Random electromagnetic reflection/scattering would repeatedly occur at the interfaces of GN skeletons, resulting in the transfer of electromagnetic energy to be dissipated as heat in the form of microcurrent. After loading of the FePc hybrid, the MA performance of composite foam displays a few recessions, as depicted in Figure 6b,e. At 2.4 mm, the RL_{min} value is −27.24 dB at 17.82 GHz and the EAB is 2.7 GHz (15.30−18 GHz). It may be attributed to the lower intrinsic attenuation characteristic of the FePc hybrid, as shown in Figure 5d. After being annealed at 800 °C for 6 h, GN/Fe@C foam exhibits more excellent MA performance than the others. As observed in Figure 6c,f, an unprecedented RL_{min} value of −72.46 dB reaches at 9.33 GHz when the thickness is controlled at 3.85 mm. At the same time, the corresponding EAB of GN/Fe@C foam can be improved to a comparative value of 4.3 GHz (from 7.68 to 12.00 GHz) with that of GN foam, covering the whole X-band. More importantly, the maximum of EAB can be extended to the wide value of 6.36 GHz (from 11.06 to 17.40 GHz). The conspicuous enhancement in MA performance can be attributed to the synergistic effect of optimized impedance matching and attenuation characteristics for GN/Fe@C foam. The result once again confirms the effectiveness of magnetic particles on the improvement in MA performance. Therefore, it can be concluded that the formation of carbon-coated iron (Fe@C) particles loaded on graphene skeletons effectively facilitate the dramatic improvement in MA performance.

Furthermore, under the same structure configuration, the MA performance of the samples can be controllably adjusted through optimizing the impedance distribution and attenuation characteristic. As depicted in Figure 7d, the attenuation constant of GN/Fe@C foams annealed at different temperatures from 600 to 1000 °C exhibits a tendency to increase. It can be ascribed to the gradually increasing pyrolysis degree of GN skeletons and FePc hybrids in foams at high temperatures. Meanwhile, the difference in the impedance gradient between GN skeletons and FePc hybrids annealed at different temperatures also endows the final foam with a unique impedance matching characteristic. As shown in Figure 7a−c, GN/Fe@C-800 foam exhibits a conspicuous optimization in impedance matching in comparison with GN/Fe@C-600 foam. The optimization may be attributed to the effective construction of a more suitable impedance gradient between

https://doi.org/10.1021/acsami.1c23439
ACS Appl. Mater. Interfaces 2022, 14, 8297−8310

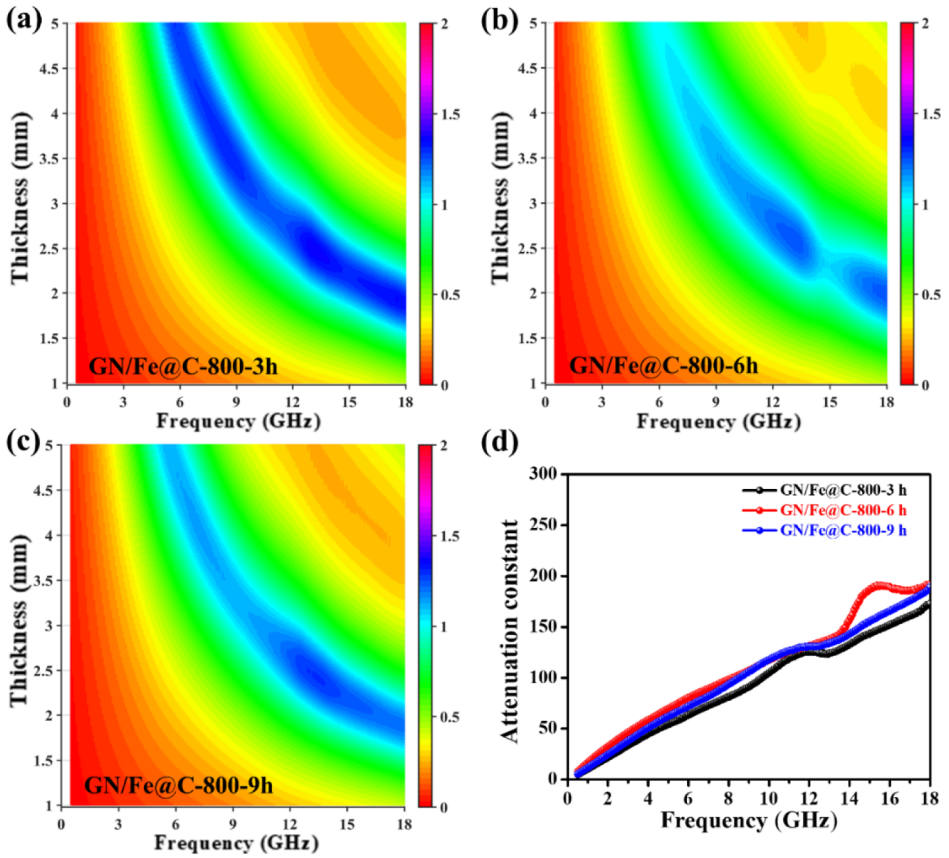

Figure 9. 2D impedance matching contour maps ($|Z_{in}/Z_o|$) of GN/Fe@C annealed at (a) 3, (b) 6, and (c) 9 h and (d) attenuation constant curves of the corresponding foams.

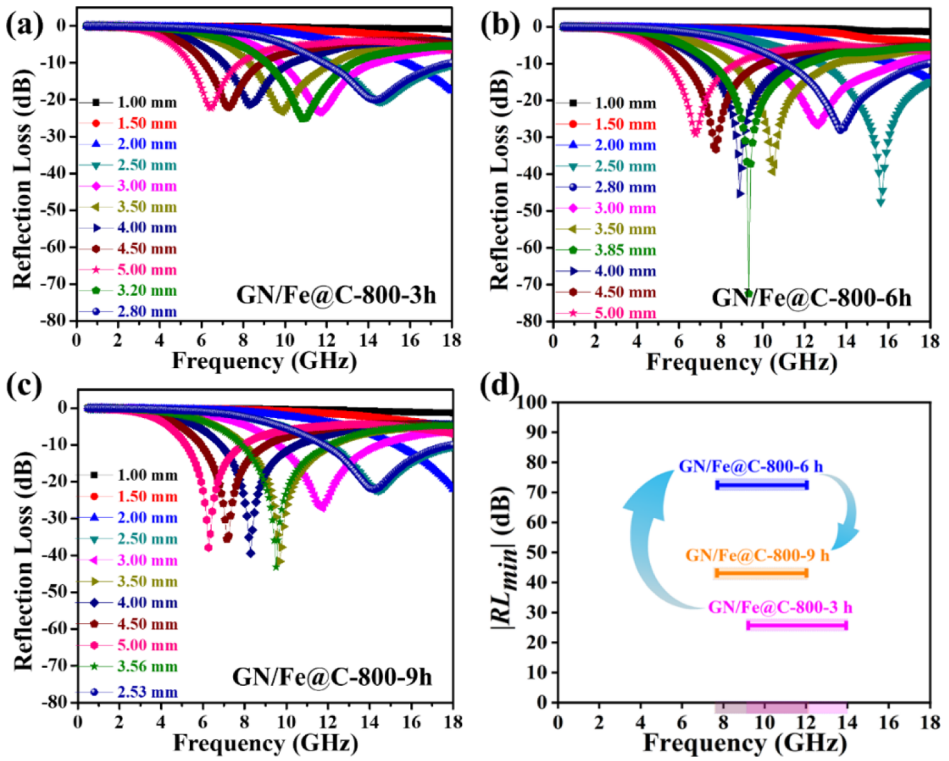

Figure 10. 2D reflection loss maps of GN/Fe@C annealed at (a) 3, (b) 6, and (c) 9 h and (d) summary of MA performance for the corresponding foams.

https://doi.org/10.1021/acsami.1c23439
ACS Appl. Mater. Interfaces 2022, 14, 8297−8310

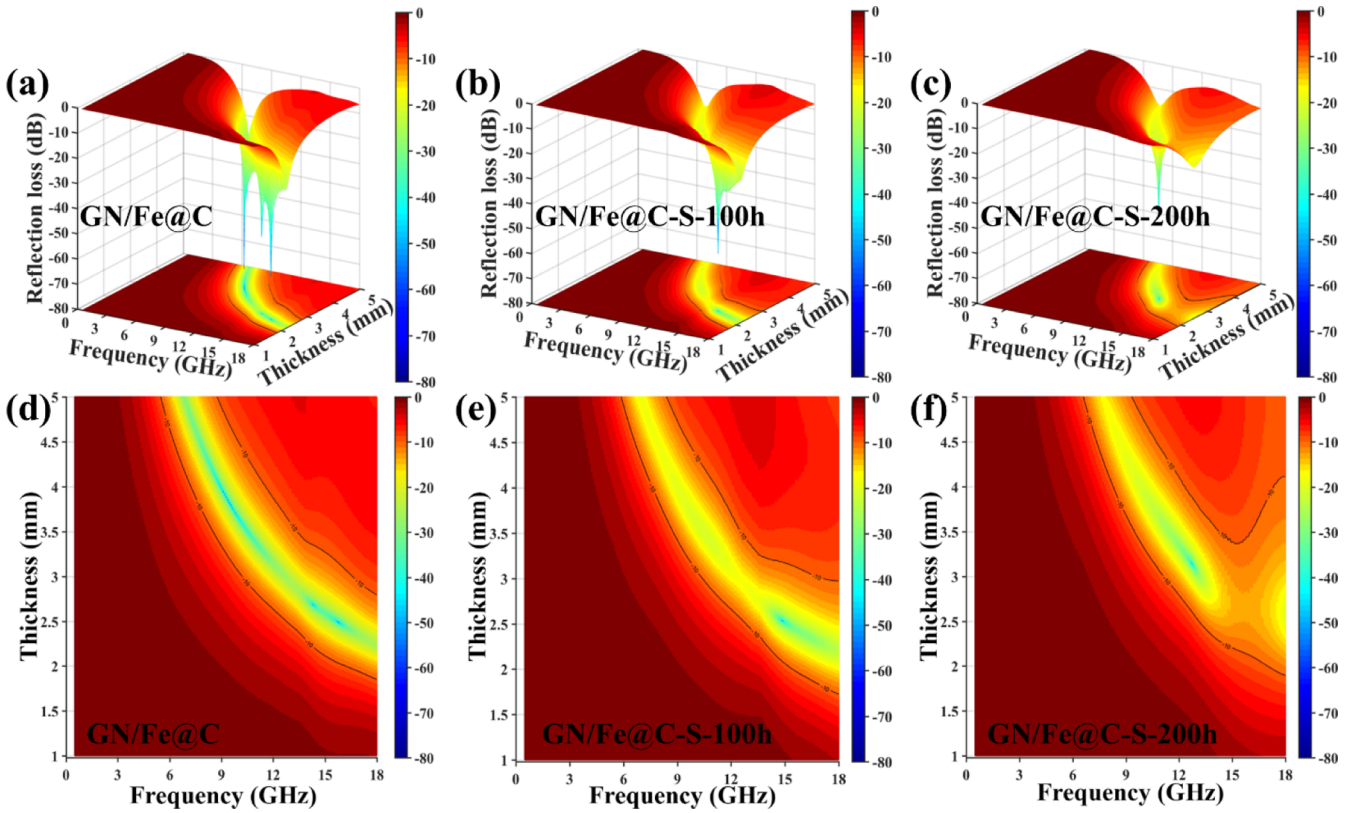

Figure 11. 3D reflection loss and contour maps of GN/Fe@C foams after the salt spray test in (a,d) 0, (b,e) 100, and (c,f) 200 h.

Fe@C and GN skeletons than that of the GN/FePc hybrid annealed at 600 °C. However, as to GN/Fe@C-1000, the corresponding impedance matching exhibits a reverse improvement owing to the excessive pyrolysis of GN skeletons and FePc hybrids in foam. It can be concluded that the pyrolysis degree of the GN skeleton and FePc hybrid in foam can be effectively adjusted by controlling annealing temperature, endowing the foams with different impedance matching. Only when the reduction degree of graphene skeleton and the pyrolysis degree of FePc hybrids are at a relatively moderate level, an excellent impedance matching performance can be achieved.

Under the synergistic effect of impedance matching and attenuation constant, the corresponding MA performances are demonstrated in Figure 8a–c. As the annealing temperature increases, the RL_{min} of foams first decreases from −46.05 to −72.46 dB and then increases to −19.17 dB. However, the corresponding EAB shows a monotonous evolution to decrease from 5.60 to 4.30 GHz and then to 1.48 GHz, as summarized in Figure 8d and Table S2. At the same time, the corresponding frequency range gradually shifts from the high-frequency Ku-band to the mid-frequency X-band and then to low-frequency C and/or S-band. The results verify the effectiveness of the annealing temperature on the optimization of MA performance. More importantly, in comparison with the final MA performances of GN/Fe@C-800 and GN/Fe@C-1000, it can be concluded that a good impedance matching plays a more crucial part than attenuation characteristic in promoting more incident electromagnetic wave to enter into the foams, thereby allowing the efficient dissipation of electromagnetic wave as much as possible.

Besides, the influence of annealing time on the MA performance was further investigated and is recorded in Figure 9. The impedance matching of those foams exhibits a tendency to be gradually optimized with the prolonging annealing time, whereas the corresponding attenuation constant of the foams first increases and then decreases, as shown in Figure 9a–d. A similar phenomenon can be observed in the complex permittivity of the foams, as shown in Figure S7. As mentioned above, many holes have been generated around magnetic Fe@C particles during the annealing treatment (Figure 1h), which are harmful to the formation of a 3D conductive network. In this case, the abnormal recession in the complex permittivity and attenuation constant of GN/Fe@C-800-9h foam may be attributed to the fact that more holes are formed on the surface of GN skeletons when the annealing time is prolonged to 9 h. As a result, the MA performance of those foams exhibits distinct diversity under the synergistic effect of impedance matching and attenuation constant.

As displayed in Figure 10 and Table S3, the RL_{min} of the foams decreases from −25.51 to −72.46 dB and then increases to −43.00 dB. Meanwhile, the EAB shows a monotonous evolution to increase from 4.12 to 4.30 GHz and then to 4.35 GHz around the mid-frequency X-band. It verified again that the controllable adjustment of MA performance can be effectively realized by optimizing annealing time.[42,43]

Corrosion Resistant Property of Composite Foams. More importantly, corrosion tests were performed for assessing the durability of the obtained GN/Fe@C foams in a neutral salt spray chamber. According to GB/T5170.2-96, the specimens were exposed to a 5 wt % NaCl solution for 100 and 200 h at a temperature of 35 °C, which were labeled GN/Fe@C-S-100h and GN/Fe@C-S-200h, respectively. As shown in Figures 11 and S8 and Table S4, the RL_{min} value of the obtained foam exhibits a conspicuous degradation from −72.46 to −56.79 dB after being treated for 100 h. As the

https://doi.org/10.1021/acsami.1c23439
ACS Appl. Mater. Interfaces 2022, 14, 8297−8310

Table 1. MA Properties of the Magnetic Porous Materials Reported Recently

	density (mg/cm^3)	RL_{min} (dB)	thickness (mm)	range (GHz)	EAB (GHz)	refs
γ-Fe_2O_3/rGO	83 wt % wax	−34.2	2.0	near 13.24	4.6	44
Fe_3O_4/ZIF-67@WA	150	−23.4	1.5	13.5−18.0	4.5	45
Ni/Carbon foam	100	−45.0	2.0	11.4−16.0	4.6	46
RGO/MWCNTs/$ZnFe_2O_4$	14.4	−52.6	1.7	12.4−16.5	4.1	47
CoNi/rGO aerogel	7.0	−53.3	0.8	14.5−18.0	3.5	21
Fe_3O_4/MWCNT/GF	5.0	−35.3	2.5	9.0−18.0	9.0	20
GN/Fe@C	11.36	−72.46	3.8	7.7−12.0	4.3	This work

testing time is prolonged to 200 h, the RL_{min} value continuously increases to a value of −47.63 dB. However, the value is still outstanding and much lower than that (−31.40 dB) of pure GN foam. Furthermore, the corresponding EAB exhibits a tendency to increase from 4.30 GHz (7.68−12.00 GHz) to 5.20 GHz (12.80−18.00 GHz) at 100 h and then to a wider value of 7.38 GHz (10.62−18.00 GHz) at 200 h. Also, the corresponding frequency range shifts from the mid-frequency X-band to the high-frequency Ku-band. After being treated at the long-time salt spray test, the retainment of such an excellent MA performance could be attributed to the formation of the carbon-coated iron (Fe@C) structure and self-cleaning surface with hydrophobicity (as demonstrated in Figure 1d,h). The synergistic effect can effectively improve the oxidation and/or corrosion resistance of magnetic particles in a harsh environment, thereby enhancing the stability and durability of GN/Fe@C foam as MA materials. Additionally, the irresistible evolution in MA capacity, bandwidth, and frequency band (as shown in Figures 11 and S8) may be ascribed to the slow corrosion of magnetic particles. The slow erosion of magnetic parts in a harsh environment makes it possible for the foams to achieve a new balance state of impedance matching and attenuation characteristic. Fortunately, a goodish MA performance could be retained. More importantly, the external surface of the GN/Fe@C foam will be loaded by sodium chloride particles after the salt spray test. As a high-dielectric material, the existence of sodium chloride fabricates the formation of a new hierarchical impedance gradient with Fe@C and the GN skeleton. As a consequence, more incident electromagnetic waves could enter the foam and be effectively dissipated, which broadens the effective absorption bandwidth of the foams as shown in Figure S8.

For comparison, Table 1 displays the recently reported magnetic porous materials and their MA performance in the frequency of 2−18 GHz.[20,21,44−47] As summarized in Table 1, GN/Fe@C foam shows a remarkable advantage compared to other materials. For instance, Shi et al. prepared a kind of homogeneous γ-Fe_2O_3 nanotube/porous reduced graphene oxide (rGO) composites using a controllable method.[44] Their RL_{min} reaches to the value of −34.20 dB with a thickness of 2.0 mm and EAB is up to 4.59 GHz. However, the magnetic γ-Fe_2O_3 nanotubes are loaded on the external surface of porous rGO skeletons. The magnetic particles were directly exposed to the air, leading to be easily oxidized and/or corroded in the harsh environment, which seriously degrades the stability and durability of MA performance. Furthermore, Fe_3O_4/ZIF-67@WA foam with a lumpish density of 150 mg/cm^3 presents an RL_{min} of −23.4 dB and an EAB of 4.5 GHz.[45] In this work, the RL_{min} of GN/Fe@C foam can achieve a better value of −72.4 dB as the corresponding density value of the foam is only an ultralow 11.36 mg/cm^3. As a result, thus excellent MA performance incorporated with a low density and corrosion resistance successfully endows GN/Fe@C foam with a great promise to be applied in marine fields.

CONCLUSIONS

In summary, novel corrosion-resistant graphene-based carbon-coated iron magnetic composite foam is successfully fabricated via self-assembly of iron phthalocyanine/Fe_3O_4 (FePc hybrid) on graphene skeletons under solvothermal conditions and then annealing at high temperature. The results of SEM, TEM, FTIR, XRD, and VSM confirm that the in situ pyrolysis of the FePc hybrid can effectively facilitate the formation of the carbon-coated iron (Fe@C) structure on the surface of graphene skeletons. Meanwhile, the successful construction of a hierarchical impedance gradient between graphene skeletons and Fe@C particles can promote the optimization in impedance matching and attenuation characteristic of the foam. Additionally, the controllable adjustment of MA performance can be effectively realized by optimizing annealing temperature and/or time. As a consequence, the optimal RL_{min} value (72.46 dB) of ultralow GN/Fe@C (11.36 mg/cm^3) can be obtained at 9.33 GHz, and the corresponding EAB is 4.30 GHz (7.68−12.00 GHz), covering the whole X-band. The maximum of EAB can be extended to the wide value of 6.36 GHz (11.06−17.40 GHz). More importantly, the formation of the carbon-coated iron structure substantially improves the corrosion resistance of magnetic particles, endowing the foam with excellent stability and durability in MA performance. After the neutral salt spray test for 200 h, the foam still processes an outstanding MA with an RL_{min} value of −47.63 dB and a wider EAB value of 7.38 GHz, which is the possibility of making GN/Fe@C foam become an efficient MA material.

ASSOCIATED CONTENT

Supporting Information

The Supporting Information is available free of charge at https://pubs.acs.org/doi/10.1021/acsami.1c23439.

Additional experimental details, materials and methods, supplementary figures for additional experimental results including TGA, TEM images, electromagnetic parameter spectra, and detailed information on the comparison table of the different GN/Fe@C foams (PDF)

AUTHOR INFORMATION

Corresponding Authors

Zicheng Wang − *The Key Laboratory of Synthetic and Biological Colloids, Ministry of Education, Institute of Nanocomposites and Energy Materials, School of Chemical and Material Engineering, Jiangnan University, 214122 Wuxi, Jiangsu, P. R. China;* orcid.org/0000-0002-8105-6908; Email: wangzc@jiangnan.edu.cn

https://doi.org/10.1021/acsami.1c23439
ACS Appl. Mater. Interfaces 2022, 14, 8297−8310

Tianxi Liu − *The Key Laboratory of Synthetic and Biological Colloids, Ministry of Education, Institute of Nanocomposites and Energy Materials, School of Chemical and Material Engineering, Jiangnan University, 214122 Wuxi, Jiangsu, P. R. China*; Email: txliu@jiangnan.edu.cn

Authors

Shuangshuang Li − *The Key Laboratory of Synthetic and Biological Colloids, Ministry of Education, Institute of Nanocomposites and Energy Materials, School of Chemical and Material Engineering, Jiangnan University, 214122 Wuxi, Jiangsu, P. R. China*

Xinwei Tang − *The Key Laboratory of Synthetic and Biological Colloids, Ministry of Education, Institute of Nanocomposites and Energy Materials, School of Chemical and Material Engineering, Jiangnan University, 214122 Wuxi, Jiangsu, P. R. China*

Yawei Zhang − *The Key Laboratory of Synthetic and Biological Colloids, Ministry of Education, Institute of Nanocomposites and Energy Materials, School of Chemical and Material Engineering, Jiangnan University, 214122 Wuxi, Jiangsu, P. R. China*

Qianqian Lan − *The Key Laboratory of Synthetic and Biological Colloids, Ministry of Education, Institute of Nanocomposites and Energy Materials, School of Chemical and Material Engineering, Jiangnan University, 214122 Wuxi, Jiangsu, P. R. China*

Zhiwei Hu − *The Key Laboratory of Synthetic and Biological Colloids, Ministry of Education, Institute of Nanocomposites and Energy Materials, School of Chemical and Material Engineering, Jiangnan University, 214122 Wuxi, Jiangsu, P. R. China*

Le Li − *The Key Laboratory of Synthetic and Biological Colloids, Ministry of Education, Institute of Nanocomposites and Energy Materials, School of Chemical and Material Engineering, Jiangnan University, 214122 Wuxi, Jiangsu, P. R. China*

Nan Zhang − *The Key Laboratory of Synthetic and Biological Colloids, Ministry of Education, Institute of Nanocomposites and Energy Materials, School of Chemical and Material Engineering, Jiangnan University, 214122 Wuxi, Jiangsu, P. R. China*

Piming Ma − *The Key Laboratory of Synthetic and Biological Colloids, Ministry of Education, Institute of Nanocomposites and Energy Materials, School of Chemical and Material Engineering, Jiangnan University, 214122 Wuxi, Jiangsu, P. R. China*

Weifu Dong − *The Key Laboratory of Synthetic and Biological Colloids, Ministry of Education, Institute of Nanocomposites and Energy Materials, School of Chemical and Material Engineering, Jiangnan University, 214122 Wuxi, Jiangsu, P. R. China*

Wengweei Tjiu − *Institute of Materials Research and Engineering, Agency for Science, Technology and Research (A*STAR), 138634, Singapore*

Complete contact information is available at: https://pubs.acs.org/10.1021/acsami.1c23439

Notes

The authors declare no competing financial interest.

ACKNOWLEDGMENTS

This work is supported by the National Natural Science Foundation of China (52003106 and 21674019), China Postdoctoral Science Foundation (2021M691265), Fundamental Research Funds for the Central Universities (2232019A3-03 and JUSRP12032), Ministry of Education of the People's Republic of China (6141A0202202), and Shanghai Scientific and Technological Innovation Project (18JC1410600).

REFERENCES

(1) Wang, B.; Wu, Q.; Fu, Y.; Liu, T. A Review on Carbon/Magnetic Metal Composites for Microwave Absorption. *J. Mater. Sci. Technol.* **2021**, *86*, 91−109.

(2) Wang, C.; Chen, P.; Li, X.; Zhu, Y.; Zhu, B. Enhanced Electromagnetic Wave Absorption for Y_2O_3-Doped SiBCN Ceramics. *ACS Appl. Mater. Interfaces* **2021**, *13*, 55440−55453.

(3) Li, W.; Li, C.; Lin, L.; Wang, Y.; Zhang, J. Foam Structure to Improve Microwave Absorption Properties of Silicon Carbide/Carbon Material. *J. Mater. Sci. Technol.* **2019**, *35*, 2658−2664.

(4) Cai, Z.; Su, L.; Wang, H.; Niu, M.; Tao, L.; Lu, D.; Xu, L.; Li, M.; Gao, H. Alternating Multilayered Si_3N_4/SiC Aerogels for Broadband and High-Temperature Electromagnetic Wave Absorption up to 1000 °C. *ACS Appl. Mater. Interfaces* **2021**, *13*, 16704−16712.

(5) Song, P.; Liu, B.; Qiu, H.; Shi, X.; Cao, D.; Gu, J. MXenes for Polymer Matrix Electromagnetic Interference Shielding Composites: A Review. *Compos. Commun.* **2021**, *24*, 100653.

(6) Wu, N.; Hu, Q.; Wei, R.; Mai, X.; Naik, N.; Pan, D.; Guo, Z.; Shi, Z. Review on the Electromagnetic Interference Shielding Properties of Carbon based Materials and their Novel Composites: Recent Progress, Challenges and Prospects. *Carbon* **2021**, *176*, 88−105.

(7) Zhang, C.; Wang, B.; Xiang, J.; Su, C.; Mu, C.; Wen, F.; Liu, Z. Microwave Absorption Properties of CoS_2 Nanocrystals Embedded into Reduced Graphene Oxide. *ACS Appl. Mater. Interfaces* **2017**, *9*, 28868−28875.

(8) Qilong, S.; Sun, L.; Cai, Y. Y.; Ye, W.; Xu, S. J.; Ji, T.; Yuan, G. Q. Fe_3O_4-intercalated Reduced Graphene Oxide Nanocomposites with Enhanced Microwave Absorption Properties. *Ceram. Int.* **2019**, *45*, 18298−18305.

(9) Zhao, J.; Zhang, J.; Wang, L.; Li, J.; Feng, T.; Fan, J.; Chen, L.; Gu, J. Superior Wave-absorbing Performances of Silicone Rubber Composites via Introducing Covalently Bonded SnO_2@MWCNT Absorbent with Encapsulation Structure. *Compos. Commun.* **2020**, *22*, 100486.

(10) Wang, Z.; Wei, R.; Liu, X. Fluffy and Ordered Graphene Multilayer Films with Improved Electromagnetic Interference Shielding Over X-band. *ACS Appl. Mater. Interfaces* **2017**, *9*, 22408−22419.

(11) Pu, L.; Li, S.; Zhang, Y.; Zhu, H.; Fan, W.; Ma, P.; Dong, W.; Wang, Z.; Liu, T. Polyimide-based Graphene Composite Foams with Hierarchical Impedance Gradient for Efficient Electromagnetic Absorption. *J. Mater. Chem. C* **2021**, *9*, 2086−2094.

(12) Chen, C.; Xi, J.; Zhou, E.; Peng, L.; Chen, Z.; Gao, C. Porous Graphene Microflowers for High-performance Microwave Absorption. *Nano−Micro Lett.* **2018**, *10*, 26.

(13) Wang, Z.; Wei, R.; Gu, J.; Liu, H.; Liu, C.; Luo, C.; Kong, J.; Shao, Q.; Wang, N.; Guo, Z.; Liu, X. Ultralight, Highly Compressible and Fire-retardant Graphene Aerogel with Self-adjustable Electromagnetic Wave Absorption. *Carbon* **2018**, *139*, 1126−1135.

(14) Zhou, Y.; Wang, S.-j.; Li, D.-s.; Jiang, L. Lightweight and Recoverable ANF/rGO/PI Composite Aerogels for Broad and High-performance Microwave Absorption. *Composites, Part B* **2021**, *213*, 108701.

(15) Qin, Y.; Zhang, Y.; Qi, N.; Wang, Q.; Zhang, X.; Li, Y. Preparation of Graphene Aerogel with High Mechanical Stability and Microwave Absorption Ability via Combining Surface Support of

Metallic-CNTs and Interfacial Cross-Linking by Magnetic Nanoparticles. *ACS Appl. Mater. Interfaces* **2019**, *11*, 10409−10417.
(16) Xu, D.; Yang, S.; Chen, P.; Yu, Q.; Xiong, X.; Wang, J. Synthesis of Magnetic Graphene Aerogels for Microwave Absorption by In-situ Pyrolysis. *Carbon* **2019**, *146*, 301−312.
(17) Zhao, B.; Li, Y.; Ji, H.; Bai, P.; Wang, S.; Fan, B.; Guo, X.; Zhang, R. Lightweight Graphene Aerogels by Decoration of 1D CoNi Chains and CNTs to Achieve Ultra-wide Microwave Absorption. *Carbon* **2021**, *176*, 411−420.
(18) Wang, X.; Lu, Y.; Zhu, T.; Chang, S.; Wang, W. $CoFe_2O_4$/N-doped Reduced Graphene Oxide Aerogels for High-performance Microwave Absorption. *Chem. Eng. J.* **2020**, *388*, 124317.
(19) Arief, I.; Biswas, S.; Bose, S. FeCo-Anchored Reduced Graphene Oxide Framework-Based Soft Composites Containing Carbon Nanotubes as Highly Efficient Microwave Absorbers with Excellent Heat Dissipation Ability. *ACS Appl. Mater. Interfaces* **2017**, *9*, 19202−19214.
(20) Shi, L.; Zhao, Y.; Li, Y.; Han, X.; Zhang, T. Octahedron Fe_3O_4 Particles Supported on 3D MWCNT/Graphene Foam: In-situ Method and Application as a Comprehensive Microwave Absorption Material. *Appl. Surf. Sci.* **2017**, *416*, 329−337.
(21) Zhao, H.-B.; Cheng, J.-B.; Zhu, J.-Y.; Wang, Y.-Z. Ultralight CoNi/rGO Aerogels Toward Excellent Microwave Absorption at Ultrathin Thickness. *J. Mater. Chem. C* **2019**, *7*, 441−448.
(22) Qiang, R.; Du, Y.; Zhao, H.; Wang, Y.; Tian, C.; Li, Z.; Han, X.; Xu, P. Metal Organic Framework-derived Fe/C Nanocubes toward Efficient Microwave Absorption. *J. Mater. Chem. A* **2015**, *3*, 13426−13434.
(23) Liu, D.; Du, Y.; Xu, P.; Wang, F.; Wang, Y.; Cui, L.; Zhao, H.; Han, X. Rationally Designed Hierarchical N-doped Carbon Nanotubes Wrapping Waxberry-like Ni@C Microspheres for Efficient Microwave Absorption. *J. Mater. Chem. A* **2021**, *9*, 5086−5096.
(24) Wang, F.; Xu, P.; Shi, N.; Cui, L.; Wang, Y.; Liu, D.; Zhao, H.; Han, X.; Du, Y. Polymer-bubbling for One-step Synthesis of Three-dimensional Cobalt/Carbon Foams against Electromagnetic Pollution. *J. Mater. Sci. Technol.* **2021**, *93*, 7−16.
(25) Du, Y.; Liu, W.; Qiang, R.; Wang, Y.; Han, X.; Ma, J.; Xu, P. Shell Thickness-dependent Microwave Absorption of Core-shell Fe_3O_4@C Composites. *ACS Appl. Mater. Interfaces* **2014**, *6*, 12997−13006.
(26) Xiang, Z.; Song, Y.; Xiong, J.; Pan, Z.; Wang, X.; Liu, L.; Liu, R.; Yang, H.; Lu, W. Enhanced Electromagnetic Wave Absorption of Nanoporous Fe_3O_4@carbon Composites Derived from Metal-organic Frameworks. *Carbon* **2019**, *142*, 20−31.
(27) Yang, X.; Lei, W.; Liu, Q.; Li, Y.; Li, K.; Wang, P.; Feng, W. A Tailor-made Method to Recycle Slow-curing Thermoset of Phthalonitrile by Constructing Self-composite with the Improved Properties. *Compos. Commun.* **2021**, *26*, 100791.
(28) Li, J.; Li, J.; Meng, H.; Xie, S.; Zhang, B.; Li, L.; Ma, H.; Zhang, J.; Yu, M. Ultra-light, Compressible and Fire-resistant Graphene Aerogel as a Highly Efficient and Recyclable Absorbent for Organic Liquids. *J. Mater. Chem. A* **2014**, *2*, 2934−2941.
(29) Qian, H.; Yu, G.; Hou, Q.; Nie, Y.; Bai, C.; Bai, X.; Wang, H.; Ju, M. Ingenious Control of Adsorbed Oxygen Species to Construct Dual Reaction Centers ZnO@FePc Photo-Fenton Catalyst with High-speed Electron Transmission Channel for PPCPs Degradation. *Appl. Catal., B* **2021**, *291*, 120064.
(30) Meng, F.; Zhao, R.; Zhan, Y.; Lei, Y.; Zhong, J.; Liu, X. Preparation and Microwave Absorption Properties of Fe-phthalocyanine Oligomer/Fe_3O_4 Hybrid Microspheres. *Appl. Surf. Sci.* **2011**, *257*, 5000−5006.
(31) Martynov, A. G.; Mack, J.; May, A. K.; Nyokong, T.; Gorbunova, Y. G.; Tsivadze, A. Y. Methodological Survey of Simplified TD-DFT Methods for Fast and Accurate Interpretation of UV-Vis-NIR Spectra of Phthalocyanines. *ACS Omega* **2019**, *4*, 7265−7284.
(32) Wu, S.; Xiong, G.; Yang, H.; Gong, B.; Tian, Y.; Xu, C.; Wang, Y.; Fisher, T.; Yan, J.; Cen, K.; Luo, T.; Tu, X.; Bo, Z.; Ostrikov, K. Multifunctional Solar Waterways: Plasma-enabled Self-cleaning Nanoarchitectures for Energy-efficient Desalination. *Adv. Energy Mater.* **2019**, *9*, 1901286.
(33) Gu, W.; Cui, X.; Zheng, J.; Yu, J.; Zhao, Y.; Ji, G. Heterostructure Design of Fe_3N Alloy/Porous Carbon Nanosheet Composites for Efficient Microwave Attenuation. *J. Mater. Sci. Technol.* **2021**, *67*, 265−272.
(34) Wang, S.; Xu, Y.; Fu, R.; Zhu, H.; Jiao, Q.; Feng, T.; Feng, C.; Shi, D.; Li, H.; Zhao, Y. Rational Construction of Hierarchically Porous Fe-Co/N-doped Carbon/rGO Composites for Broadband Microwave Absorption. *Nano−Micro Lett.* **2019**, *11*, 76.
(35) Dong, S.; Zhang, X.; Li, X.; Chen, J.; Hu, P.; Han, J. SiC Whiskers-reduced Graphene Oxide Composites Decorated with MnO Nanoparticles for Tunable Microwave Absorption. *Chem. Eng. J.* **2020**, *392*, 123817.
(36) Zhang, Z.; Cai, Z.; Xia, L.; Zhao, D.; Fan, F.; Huang, Y. Synergistically Assembled Cobalt-Telluride/Graphene Foam with High-Performance Electromagnetic Wave Absorption in Both Gigahertz and Terahertz Band Ranges. *ACS Appl. Mater. Interfaces* **2021**, *13*, 30967−30979.
(37) Wu, C.; Chen, Z.; Wang, M.; Cao, X.; Zhang, Y.; Song, P.; Zhang, T.; Ye, X.; Yang, Y.; Gu, W.; Zhou, J.; Huang, Y. Confining Tiny MoO_2 Clusters into Reduced Graphene Oxide for Highly Efficient Low Frequency Microwave Absorption. *Small* **2020**, *16*, 2001686.
(38) Cui, E.; Pan, F.; Xiang, Z.; Liu, Z.; Yu, L.; Xiong, J.; Li, X.; Lu, W. Engineering Dielectric Loss of FeCo/Polyvinylpyrrolidone Core-shell Nanochains@Graphene Oxide Composites with Excellent Microwave Absorbing Properties. *Adv. Eng. Mater.* **2021**, *23*, 2000827.
(39) Zhang, Y.; Li, S.; Tang, X.; Fan, W.; Lan, Q.; Li, L.; Ma, P.; Dong, W.; Wang, Z.; Liu, T. Ultralight and Ordered Lamellar Polyimide-based Graphene Foams with Efficient Broadband Electromagnetic Absorption. *J. Mater. Sci. Technol.* **2022**, *102*, 97−104.
(40) Li, Q.; Tian, X.; Yang, W.; Hou, L.; Li, Y.; Jiang, B.; Wang, X.; Li, Y. Fabrication of Porous Graphene-like Carbon Nanosheets with Rich Doped-nitrogen for High-performance Electromagnetic Microwave Absorption. *Appl. Surf. Sci.* **2020**, *530*, 147298.
(41) Meng, X.; Lei, W.; Yang, W.; Liu, Y.; Yu, Y. Fe_3O_4 Nanoparticles Coated with Ultra-thin Carbon Layer for Polarization-controlled Microwave Absorption Performance. *J. Colloid Interface Sci.* **2021**, *600*, 382−389.
(42) Li, Y.; Cheng, H.; Wang, N.; Zhou, Y.; Li, T. Magnetic and Microwave Absorption Properties of Fe/TiO2 Nanocomposites Prepared by Template Electrodeposition. *J. Alloys Compd.* **2018**, *763*, 421−429.
(43) Zhang, X.-J.; Zhu, J.-Q.; Yin, P.-G.; Guo, A.-P.; Huang, A.-P.; Guo, L.; Wang, G.-S. Tunable High-performance Microwave Absorption of $Co_{1-x}S$ Hollow Spheres Constructed by Nanosheets within Ultralow Filler Loading. *Adv. Funct. Mater.* **2018**, *28*, 1800761.
(44) Wang, S.; Jiao, Q.; Liu, X.; Xu, Y.; Shi, Q.; Yue, S.; Zhao, Y.; Liu, H.; Feng, C.; Shi, D. Controllable Synthesis of γ-Fe_2O_3 Nanotube/Porous rGO Composites and Their Enhanced Microwave Absorption Properties. *ACS Sustainable Chem. Eng.* **2019**, *7*, 7004−7013.
(45) Xu, L.; Xiong, Y.; Dang, B.; Ye, Z.; Jin, C.; Sun, Q.; Yu, X. In-situ Anchoring of Fe_3O_4/ZIF-67 Dodecahedrons in Highly Compressible Wood Aerogel with Excellent Microwave Absorption Properties. *Mater. Des.* **2019**, *182*, 108006.
(46) Zhao, H.-B.; Fu, Z.-B.; Chen, H.-B.; Zhong, M.-L.; Wang, C.-Y. Excellent Electromagnetic Absorption Capability of Ni/Carbon Based Conductive and Magnetic Foams Synthesized via a Green One Pot Route. *ACS Appl. Mater. Interfaces* **2016**, *8*, 1468−1477.
(47) Li, N.; Shu, R.; Zhang, J.; Wu, Y. Synthesis of Ultralight Three-dimensional Nitrogen-doped Reduced Graphene Oxide/Multi-walled Carbon Nanotubes/Zinc Ferrite Composite Aerogel for Highly Efficient Electromagnetic Wave Absorption. *J. Colloid Interface Sci.* **2021**, *596*, 364−375.

https://doi.org/10.1021/acsami.1c23439
ACS Appl. Mater. Interfaces 2022, 14, 8297−8310